Editors' Suggestion

Sublattice Structure and Topology in Spontaneously Crystallized Electronic States

Yongxin Zeng,[1,*] Daniele Guerci,[2] Valentin Crépel,[2] Andrew J. Millis,[1,2] and Jennifer Cano[3,2]
[1]Department of Physics, Columbia University, New York, New York 10027, USA
[2]Center for Computational Quantum Physics, Flatiron Institute, New York, New York 10010, USA
[3]Department of Physics and Astronomy, Stony Brook University, Stony Brook, New York 11794, USA

(Received 11 March 2024; revised 13 May 2024; accepted 16 May 2024; published 7 June 2024)

The prediction and realization of the quantum anomalous Hall effect are often intimately connected to honeycomb lattices in which the sublattice degree of freedom plays a central role in the nontrivial topology. Two-dimensional Wigner crystals, on the other hand, form triangular lattices without sublattice degrees of freedom, resulting in a topologically trivial state. Here, we discuss the possibility of spontaneously formed honeycomb-lattice crystals that exhibit the quantum anomalous Hall effect. Starting from a single-band system with nontrivial quantum geometry, we derive the mean-field energy functional of a class of crystal states and express it as a model of sublattice pseudospins in momentum space. We find that nontrivial quantum geometry leads to extra terms in the pseudospin model that break an effective "time-reversal symmetry" and favor a topologically nontrivial pseudospin texture. When the effects of these extra terms dominate over the ferromagnetic exchange coupling between pseudospins, the anomalous Hall crystal state becomes energetically favorable over the trivial Wigner crystal state.

DOI: 10.1103/PhysRevLett.132.236601

Introduction.—Topology and spontaneously broken symmetry are two central themes of modern condensed matter physics. One prototypical broken symmetry phase is the Wigner crystal (WC) [1], a phase characterized by spontaneously broken translational invariance and trivial topology. In two dimensions (2D), semiclassical calculations in the low-density limit predict [2] that the lowest energy configuration of electrons moving in a uniform positive background and interacting via the conventional Coulomb interaction is a triangular-lattice Wigner crystal. Theoretical and experimental studies [3–14] over the past few decades have established Wigner crystals as one of the prototypical broken symmetry states of strongly interacting electron systems.

The quantum anomalous Hall (QAH) insulator [15] is a topologically nontrivial insulating state that exhibits a quantized Hall conductance in the absence of an external magnetic field. First predicted by Haldane in a honeycomb-lattice model [16], it has been realized experimentally in magnetic topological insulators [17–19] and more recently in moiré superlattices [20–25] where the low-energy QAH physics can often be understood via a mapping to the Haldane model in a honeycomb superlattice [26–28].

The sublattice degree of freedom is crucial for the nontrivial topology of QAH insulators in honeycomb lattices. In fact, it has been shown [29–35] that when a honeycomb-superlattice modulation is applied to a gapped 2D system with nontrivial band geometry, the lowest miniband is topologically nontrivial under mild assumptions. Interaction-driven topological insulating states have also been discussed in the context of honeycomb lattices [36–39]. In these cases, translation invariance is explicitly broken. The question of the circumstances under which a *spontaneously broken* translation invariance may lead to a topologically nontrivial QAH state remains open.

The coexistence of spontaneously broken translation invariance and conventional (magnetic field induced) quantum Hall effects was discussed in pioneering papers by Halperin and co-workers [40,41]. This Letter was a proof of principle, based on a model with specifically tuned interactions. The possibility of a spontaneously formed crystal phase that exhibits the QAH effect in zero applied field, however, has apparently not been considered until very recently. Following the discovery of integer and fractional QAH effects in rhombohedral pentalayer graphene aligned to a hexagonal boron nitride substrate [23–25], mean-field calculations found [42–46] a robust QAH insulator state at filling factor $\nu = 1$. The experimental devices involved a moiré potential that explicitly broke the translational invariance and the theoretical studies therefore were based on models that also explicitly broke translation invariance. Surprisingly, the QAH insulator state was found theoretically to persist in the limit of vanishing moiré potential, implying that a spontaneous translational symmetry breaking could lead to an "anomalous Hall crystal" (AHC) state.

In this Letter we investigate theoretically the circumstances under which a topologically nontrivial electron crystal may occur. We use a simple yet general model based a single band of electrons that we view as representing the low-energy physics of a multiband system. The quantum geometry appears in the Hamiltonian as form factors in the

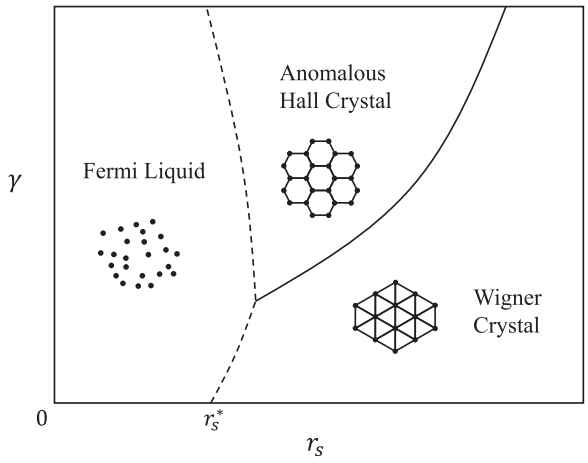

FIG. 1. Schematic phase diagram in the plane of interaction strength r_s and Berry curvature concentration γ showing regions of Fermi liquid, conventional Wigner crystal, and anomalous Hall crystal phases. The precise definitions of r_s and γ are provided in a later part of the paper. $r_s^* \approx 30$ is the critical interaction strength for the Wigner crystallization phase transition in systems with trivial quantum geometry [3,4]. Our theory focuses on the transition between two crystal phases (solid line); melting of crystals is not explicitly considered in our theory and the dashed line is speculation based on the Lindemann criterion.

projection of Coulomb interactions onto the low-energy band. We use this Hamiltonian to study the energetic competition between WC and AHC states. Crucial to our analysis is the observation that the WC and AHC states have the same Bravais lattice but different sublattice structures. This enables the construction of a sublattice pseudospin representation of the physics that provides an interpolation between the topologically trivial WC and nontrivial AHC states. Combining analytic derivation of a sublattice pseudospin model and numerical self-consistent mean-field calculations, we find that AHCs are stabilized by strong enough Berry curvature concentration at intermediate interaction strengths, implying the phase diagram shown in Fig. 1.

Model.—We consider a 2D electron system described by a single band with arbitrary dispersion consistent with C_6 symmetry and nontrivial quantum geometry described by the Hamiltonian $H = H_{\text{kin}} + H_{\text{int}}$. The kinetic energy is

$$H_{\text{kin}} = \sum_{\boldsymbol{p}} E_{\boldsymbol{p}} c_{\boldsymbol{p}}^\dagger c_{\boldsymbol{p}}, \tag{1}$$

where $E_{\boldsymbol{p}}$ is the band dispersion and $c_{\boldsymbol{p}}$ ($c_{\boldsymbol{p}}^\dagger$) is the annihilation (creation) operator of electrons with momentum $\boldsymbol{p}$. We view $E_{\boldsymbol{p}}$ as the lowest-lying band of a multiband system and the momentum $\boldsymbol{p}$ runs over the large Brillouin zone of the microscopic lattice describing this multiband system. Because the physics of interest involves a low density of electrons in this band, leading to a long-period superlattice, we may treat the large Brillouin zone as an infinite 2D momentum space. Interactions between electrons are described by the Hamiltonian,

$$H_{\text{int}} = \frac{1}{2\mathcal{A}} \sum_{\boldsymbol{p}\boldsymbol{p}'\boldsymbol{q}} V_{\boldsymbol{q}} \Lambda_{\boldsymbol{p}+\boldsymbol{q},\boldsymbol{p}} \Lambda_{\boldsymbol{p}',\boldsymbol{p}'+\boldsymbol{q}} c_{\boldsymbol{p}+\boldsymbol{q}}^\dagger c_{\boldsymbol{p}'}^\dagger c_{\boldsymbol{p}'+\boldsymbol{q}} c_{\boldsymbol{p}}, \tag{2}$$

where $\mathcal{A}$ is the area of the 2D system. Anticipating the honeycomb-lattice structure of spontaneously formed crystals, we require that both $E_{\boldsymbol{p}}$ and $V_{\boldsymbol{q}}$ preserve C_6 rotational symmetry. The quantum geometry is encoded in the form factor $\Lambda_{\boldsymbol{p}',\boldsymbol{p}} = \langle u_{\boldsymbol{p}'} | u_{\boldsymbol{p}} \rangle$, where $|u_{\boldsymbol{p}}\rangle$ is the periodic part of the Bloch wave function of the projected band. C_6 symmetry imposes the constraint $\Lambda_{C_6\boldsymbol{p}',C_6\boldsymbol{p}} = \Lambda_{\boldsymbol{p}',\boldsymbol{p}}$. For a trivial band with vanishing Berry curvature, $\Lambda_{\boldsymbol{p}',\boldsymbol{p}} \in \mathbb{R}$ by a proper gauge choice. This implies an emergent $C_2\mathcal{T}$ symmetry where $\mathcal{T}$ is an effective "time-reversal" operator [47]. For a generic band with nontrivial quantum geometry, $\Lambda_{\boldsymbol{p}',\boldsymbol{p}}$ is in general complex and the effective time-reversal symmetry (TRS) [48] is broken.

The Hartree-Fock potential defines a Bravais lattice common to both the WC and AHC states, which are distinguished by different sublattice structures. We may view the triangular lattice WC as the state with one sublattice of the AHC honeycomb occupied and the other one empty. We are interested in the lowest-lying bands of the long-period superlattice; these are defined in terms of the original microscopic states via the sublattice basis $a_{\boldsymbol{k}}^\dagger = \sum_{\boldsymbol{g}} A_{\boldsymbol{k}+\boldsymbol{g}} c_{\boldsymbol{k}+\boldsymbol{g}}^\dagger$ and $b_{\boldsymbol{k}}^\dagger = \sum_{\boldsymbol{g}} B_{\boldsymbol{k}+\boldsymbol{g}} c_{\boldsymbol{k}+\boldsymbol{g}}^\dagger$, where $A_{\boldsymbol{p}}, B_{\boldsymbol{p}}$ are momentum-space wave functions of the localized sublattice orbitals and $\boldsymbol{g}$ sums over reciprocal lattice vectors of the long-period superlattice whose lattice constant is determined by the electron density. To comply with the point-group symmetries of the honeycomb lattice, each sublattice basis state has TRS and C_3 rotational symmetry around its center, and the two sublattices are related by C_2 rotation around the hexagon center (see Supplemental Material [49] for details). A general Hartree-Fock ground state is a superposition of two sublattice basis states:

$$|\Psi\rangle = \prod_{\boldsymbol{k}\in \text{mBZ}} \left(\cos\frac{\theta_{\boldsymbol{k}}}{2} a_{\boldsymbol{k}}^\dagger + e^{i\phi_{\boldsymbol{k}}} \sin\frac{\theta_{\boldsymbol{k}}}{2} b_{\boldsymbol{k}}^\dagger \right) |0\rangle. \tag{3}$$

Here $|0\rangle$ is the vacuum state and $\boldsymbol{k}$ runs over the mini Brillouin zone (mBZ) of the long-period superlattice. The polar and azimuthal angles $(\theta_{\boldsymbol{k}}, \phi_{\boldsymbol{k}})$ define a *sublattice pseudospin* at each momentum site in the mBZ that can be alternatively represented by a unit vector:

$$\boldsymbol{n}_{\boldsymbol{k}} = (\sin\theta_{\boldsymbol{k}} \cos\phi_{\boldsymbol{k}}, \sin\theta_{\boldsymbol{k}} \sin\phi_{\boldsymbol{k}}, \cos\theta_{\boldsymbol{k}}). \tag{4}$$

In the language of sublattice pseudospins, triangular-lattice WCs correspond to out-of-plane polarized states (e.g., $\theta_{\boldsymbol{k}} \approx 0$) and honeycomb-lattice AHCs are states in which the pseudospins form a skyrmion texture in the mBZ and the net out-of-plane polarization vanishes. The pseudospin texture and the precise forms of the sublattice basis states are obtained by variational minimization of energy $\langle\Psi|H|\Psi\rangle$.

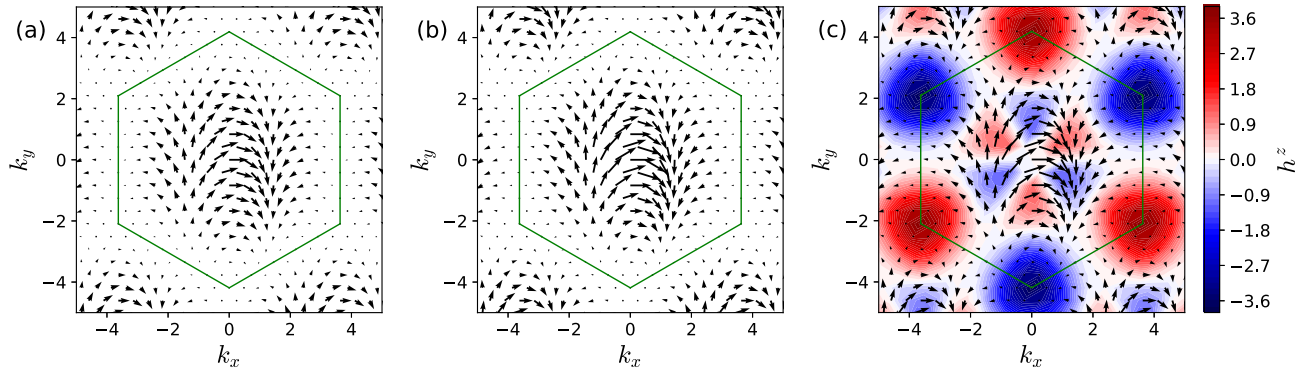

FIG. 2. Pseudospin Zeeman field $\boldsymbol{h}_{\boldsymbol{k}}$ in units of the kinetic energy scale $\mathcal{E}_{\mathrm{kin}}$. The arrows represent the in-plane components $(h^x_{\boldsymbol{k}}, h^y_{\boldsymbol{k}})$, scaled down by a factor of 40 and plotted on the axis scale, and the colors represent the out-of-plane component $h^z_{\boldsymbol{k}}$. The green hexagon shows the mBZ boundary. Panel (a) shows the kinetic energy part and panels (b) and (c) show the Hartree-Fock part at $\gamma = 0$ and $\gamma = 0.4$, respectively. Other parameters used in the calculations include localization length $l = 0.25$, interaction strength $r_s = 20$, and winding number $N = 3$.

The Chern number of the ground state $|\Psi\rangle$ is given by the winding of $\boldsymbol{n}_{\boldsymbol{k}}$:

$$C = \int_{\mathrm{mBZ}} \frac{d^2\boldsymbol{k}}{4\pi} \boldsymbol{n}_{\boldsymbol{k}} \cdot (\partial_{k_x} \boldsymbol{n}_{\boldsymbol{k}} \times \partial_{k_y} \boldsymbol{n}_{\boldsymbol{k}}). \tag{5}$$

The WC state has $C = 0$ and the AHC state has $C = \pm 1$ depending on the pseudospin texture.

Pseudospin order.—To compare the energy of states with different sublattice pseudospin order, we calculate the energy expectation value of a generic state of the form given in Eq. (3). Up to a constant energy independent of pseudospin texture, the mean-field (MF) energy functional takes the form [53,54]

$$E_{\mathrm{MF}}[\theta, \phi] \equiv \langle \Psi | H | \Psi \rangle = -\sum_{\boldsymbol{k}} \boldsymbol{h}_{\boldsymbol{k}} \cdot \boldsymbol{n}_{\boldsymbol{k}} - \frac{1}{2} \sum_{\alpha\beta} \sum_{\boldsymbol{k}\boldsymbol{k}'} J^{\alpha\beta}_{\boldsymbol{k}\boldsymbol{k}'} n^{\alpha}_{\boldsymbol{k}} n^{\beta}_{\boldsymbol{k}'}, \tag{6}$$

where the α, β indices run over Cartesian coordinates x, y, z. The problem is thus transformed into an effective spin model in momentum space: $\boldsymbol{h}_{\boldsymbol{k}}$ is an effective Zeeman field that acts on sublattice pseudospins, and $J^{\alpha\beta}_{\boldsymbol{k}\boldsymbol{k}'} = J^{\beta\alpha}_{\boldsymbol{k}'\boldsymbol{k}}$ are coupling coefficients between pseudospins at different momentum sites. While the full expressions of $\boldsymbol{h}_{\boldsymbol{k}}$ and $J^{\alpha\beta}_{\boldsymbol{k}\boldsymbol{k}'}$ are lengthy (see Supplemental Material [49]), the symmetry analysis and physical arguments given below make their qualitative features clear.

The pseudospin Zeeman field has contributions from both the bare kinetic energy and the interactions; physically, the interaction contribution to $\boldsymbol{h}_{\boldsymbol{k}}$ arises from the Hartree-Fock potential produced by the average electron distribution. Because the average charge density is honeycomb shaped, the mean-field potential is C_6 symmetric. Analogous to graphene, when TRS is preserved, all $\boldsymbol{h}_{\boldsymbol{k}}$ are in plane ($h^z_{\boldsymbol{k}} = 0$) and form vortices of opposite chirality around the Dirac points K and K'. See Supplemental Material [49] for a proof by symmetry analysis and Figs. 2(a) and 2(b) for graphical representations.

In addition to pseudospin Zeeman fields, interactions also give rise to coupling between pseudospins. In the limit of small $|\boldsymbol{k} - \boldsymbol{k}'| \ll a^{-1}$, where a is the superlattice constant, the dominant coupling coefficients are

$$J^{xx}_{\boldsymbol{k}\boldsymbol{k}'} \approx J^{yy}_{\boldsymbol{k}\boldsymbol{k}'} \approx J^{zz}_{\boldsymbol{k}\boldsymbol{k}'} \approx \frac{1}{2A} V_{\boldsymbol{k}'-\boldsymbol{k}}, \tag{7}$$

which represent Heisenberg ferromagnetic coupling between pseudospins. Next-order expansion suggests that out-of-plane coupling J^{zz} is slightly stronger than in-plane coupling J^{xx}, J^{yy}. Since the pseudospin texture that follows $\boldsymbol{h}_{\boldsymbol{k}}$ (i.e., $\boldsymbol{n}_{\boldsymbol{k}} = \boldsymbol{h}_{\boldsymbol{k}}/|\boldsymbol{h}_{\boldsymbol{k}}|$) is singular around the Dirac points and leads to high exchange energy cost, spontaneous breaking of sublattice symmetry occurs when interactions get strong. Thus, in the strong-interaction limit (large-r_s limit in Fig. 1), all electrons are polarized to one of the sublattices, forming a triangular-lattice WC.

A similar mean-field theory study has been carried out in the context of graphene [53,54], where an explicit translational symmetry breaking occurs due to the periodic lattice potential of graphene. Our case differs from these previous works in two important ways. Because of the absence of explicit translational symmetry breaking, the graphenelike state in the weak-interaction limit where kinetic energy dominates is likely an artifact of the sublattice basis construction and the true ground state is a Fermi liquid. More importantly, in the presence of nontrivial quantum geometry, we find that spontaneous breaking of translational symmetry leads to a topologically nontrivial honeycomb-lattice state—the AHC state—in a range of intermediate interaction strength.

Effects of quantum geometry.—TRS combined with C_2 rotational symmetry guarantees invariance of energy with respect to sublattice inversion $n^z_{\boldsymbol{k}} \to -n^z_{\boldsymbol{k}}$ and therefore vanishing of h^z, J^{zx}, and J^{zy}. When TRS is broken by

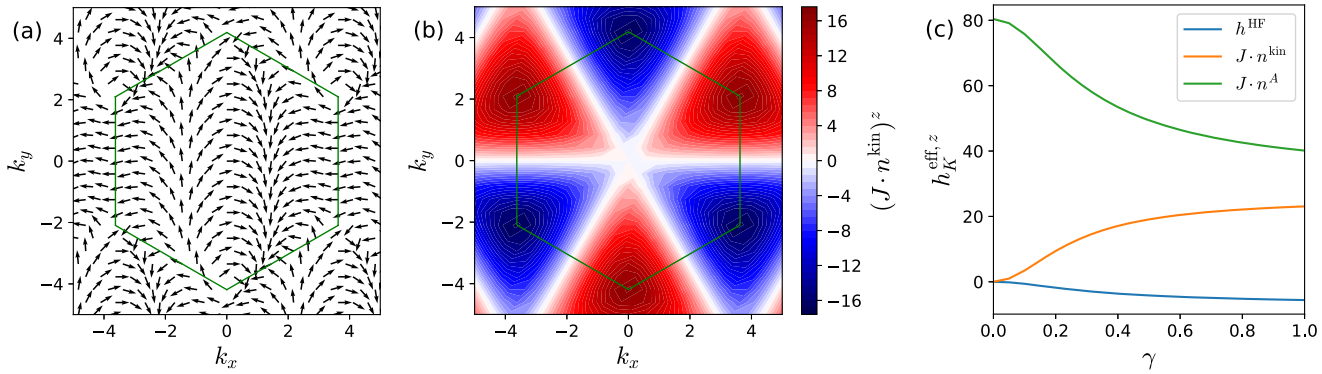

FIG. 3. (a) Pseudospin texture that follows the kinetic energy part of Zeeman field $\boldsymbol{n}_{\boldsymbol{k}}^{\mathrm{kin}} = \boldsymbol{h}_{\boldsymbol{k}}^{\mathrm{kin}}/|\boldsymbol{h}_{\boldsymbol{k}}^{\mathrm{kin}}|$. (b) Effective out-of-plane Zeeman field generated by the pseudospins in (a) at $\gamma = 0.4$. (c) Effective out-of-plane Zeeman field at K point as a function of γ. The blue curve represents the Hartree-Fock part of Zeeman field $h_K^{\mathrm{HF},z}$, and the orange and green curves respectively represent the effective field generated by $\boldsymbol{n}_{\boldsymbol{k}}^{\mathrm{kin}}$ and the one generated by the sublattice-polarized state $\boldsymbol{n}_{\boldsymbol{k}}^{A} = (0, 0, 1)$. Other parameters used in the calculations include $l = 0.25$, $r_s = 20$, and $N = 3$.

nontrivial form factors, all coefficients are generically nonzero. A nonzero h^z explicitly gaps out the Dirac cones at K and K'. In addition, J^{zx}, J^{zy} couplings together with the in-plane components of pseudospins n^x, n^y effectively generate another out-of-plane Zeeman field. C_2 symmetry implies that the z component of the net effective Zeeman field is opposite at two Dirac points. The pseudospin texture that is aligned with the effective Zeeman field thus forms a topologically nontrivial skyrmion texture in the mBZ. If $n_K^z = +1$ and $n_{K'}^z = -1$, the Chern number is $C = +1$; the opposite case $n_K^z = -1$, $n_{K'}^z = +1$ leads to $C = -1$. The locally smooth pseudospin texture also implies lower exchange energy cost and higher stability against sublattice-polarized states. Overall, TRS breaking makes the topologically nontrivial AHC state more favorable.

To make the analysis quantitative, we now provide an explicit example where the AHC is stabilized for sufficient TRS breaking. We assume quadratic dispersion $E_{\boldsymbol{p}} = \hbar^2 p^2/2m$ and gate-screened Coulomb interaction $V_{\boldsymbol{q}} = (2\pi e^2/q)\tanh(qd/2)$, where d is the distance to gate. In terms of lattice constant a (an input parameter determined by electron density), the kinetic energy scale is $\mathcal{E}_{\mathrm{kin}} = \hbar^2/2ma^2$ and the interaction energy scale is $\mathcal{E}_{\mathrm{int}} = e^2/a$. Below we express all lengths in units of a and energies in units of $\mathcal{E}_{\mathrm{kin}}$, and introduce the r_s parameter by $\pi(r_s\hbar^2/me^2)^2 = \sqrt{3}a^2/2$. In this language, $\mathcal{E}_{\mathrm{int}} = r_s\sqrt{8\pi/\sqrt{3}}$. Since d is a constant length independent of a, $d/a \propto 1/r_s$. In our calculations we take $d/a = 50/r_s$ [55].

The sublattice basis states in the variational wave function (3) are constructed by solving the problem of an electron moving in a honeycomb-lattice potential in the plane-wave basis and Wannierizing the lowest two bands (see Supplemental Material [49] for details). The potential strength controls the localization length l of the constructed basis states.

To model a band with nontrivial quantum geometry, we take the Bloch wave function $|u_{\boldsymbol{p}}\rangle$ as a two-component spinor in the basis of internal microscopic orbitals. Partly motivated by recent work on rhombohedral multilayer graphene [42–46], we take $|u_{\boldsymbol{p}}\rangle = [\cos(\alpha_{\boldsymbol{p}}/2), e^{i\beta_{\boldsymbol{p}}}\sin(\alpha_{\boldsymbol{p}}/2)]$, where $\alpha_{\boldsymbol{p}} = \arctan(\gamma|\boldsymbol{p}|)$ and $\beta_{\boldsymbol{p}} = N\arg(p_x + ip_y)$. Here $N \in \mathbb{Z}_+$ is the winding number and emulates the number of graphene layers, while $\gamma \geq 0$ describes the concentration of Berry curvature near the origin. Since momentum is measured in units of the long-period superlattice constant, when $\gamma \sim 1$ Berry curvature is concentrated on the scale of the mBZ. We use $N = 3$ for our calculations below unless otherwise stated, although qualitatively similar results are also observed for other winding numbers, as shown in the Supplemental Material [49].

Figure 2 shows the pseudospin Zeeman fields $\boldsymbol{h}_{\boldsymbol{k}}$ computed with a pair of sublattice basis states with localization length $l = 0.25$. The kinetic energy part $\boldsymbol{h}_{\boldsymbol{k}}^{\mathrm{kin}}$ [Fig. 2(a)] is independent of form factors. C_6 symmetry dictates that it is all in plane and forms vortices of opposite chirality around $K = (2\pi/\sqrt{3}, 2\pi/3)$ and $K' = -K$. When the form factor is trivial ($\gamma = 0$), the Hartree-Fock (HF) part $\boldsymbol{h}_{\boldsymbol{k}}^{\mathrm{HF}}$ [Fig. 2(b)] forms a similar in-plane pattern as the kinetic part. As γ increases and breaks TRS, $\boldsymbol{h}_{\boldsymbol{k}}^{\mathrm{HF}}$ gains an out-of-plane component that is opposite at K and K'. See Fig. 2(c) for the case of $\gamma = 0.4$.

In the mean-field picture, coupling between pseudospins generates an effective Zeeman field $h_{\boldsymbol{k}}^{\mathrm{eff},\alpha} = \sum_{\beta,\boldsymbol{k}'} J_{\boldsymbol{k}\boldsymbol{k}'}^{\alpha\beta} n_{\boldsymbol{k}'}^{\beta}$ that depends on the pseudospin texture. To see how J^{zx} and J^{zy} couplings lead to a topologically nontrivial state, we consider the in-plane pseudospin texture that follows the kinetic Zeeman field $\boldsymbol{n}_{\boldsymbol{k}}^{\mathrm{kin}} = \boldsymbol{h}_{\boldsymbol{k}}^{\mathrm{kin}}/|\boldsymbol{h}_{\boldsymbol{k}}^{\mathrm{kin}}|$ [Fig. 3(a)] and calculate the out-of-plane Zeeman field it generates in the mBZ:

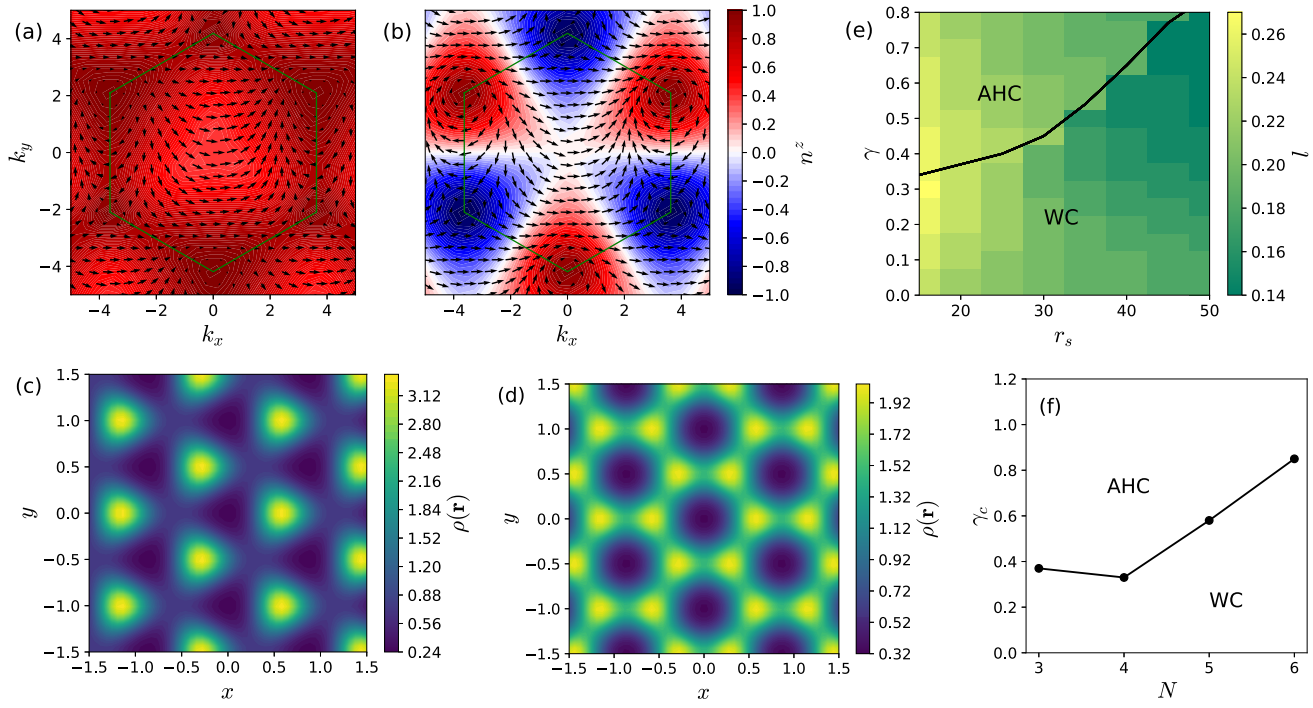

FIG. 4. (a),(b) Sublattice pseudospin textures of the ground states at $r_s = 20$ and (a) $\gamma = 0.3$, (b) $\gamma = 0.4$. The winding number is $N = 3$ for (a)–(e). (c),(d) Charge density distribution of the states in (a) and (b). (e) Phase diagram as a function of r_s and γ. The color scale represents the localization length l of the ground state, and the black curve separates the trivial Wigner crystal (WC) and $C = 1$ anomalous Hall crystal (AHC) states. (f) The critical value of γ for different winding numbers N at $r_s = 20$.

$$h_{\boldsymbol{k}}^{\mathrm{eff},z} = \sum_{\boldsymbol{k}'} (J_{\boldsymbol{k}\boldsymbol{k}'}^{zx} n_{\boldsymbol{k}'}^{\mathrm{kin},x} + J_{\boldsymbol{k}\boldsymbol{k}'}^{zy} n_{\boldsymbol{k}'}^{\mathrm{kin},y}) \equiv (J \cdot n^{\mathrm{kin}})_{\boldsymbol{k}}^{z}. \quad (8)$$

As shown in Fig. 3(b), the effective field is an odd function of $\boldsymbol{k}$. Comparison between Figs. 2(c) and 3(b) shows that $\boldsymbol{h}^{\mathrm{HF}}$ and $J \cdot n^{\mathrm{kin}}$ have opposite effects on the sublattice polarization at K and K' points and thus push toward opposite AHC states [56]; $\boldsymbol{h}^{\mathrm{HF}}$ alone leads to a $C = -1$ state while $J \cdot n^{\mathrm{kin}}$ favors $C = +1$. Because $(J \cdot n^{\mathrm{kin}})^z$ has much larger amplitude than $h^{\mathrm{HF},z}$, we expect that the overall energetically favorable state has $C = +1$.

In Fig. 3(c) we plot the z component of $\boldsymbol{h}^{\mathrm{HF}}$ and $J \cdot n^{\mathrm{kin}}$ fields at K as a function of γ. We find that the amplitude of both fields monotonically increases with γ, with the latter always several times larger than the former. In the same figure we also plot another quantity that measures the out-of-plane ferromagnetic coupling strength:

$$(J \cdot n^{A})_{K}^{z} \equiv \sum_{\boldsymbol{k}} J_{\boldsymbol{K}\boldsymbol{k}}^{zz}. \quad (9)$$

Physically this is the effective out-of-plane Zeeman field at K produced by the A-sublattice polarized state $\boldsymbol{n}_{\boldsymbol{k}}^{A} = (0, 0, 1)$. We find that the ferromagnetic coupling strength is significantly reduced as γ increases from 0 to 1. Weakening of ferromagnetic coupling increases the energy of sublattice-polarized states and further stabilizes the AHC state that is favored by the effective pseudospin Zeeman fields.

Phase diagram.—To find the mean-field ground state of the system, we project the system Hamiltonian onto the two-sublattice subspace and perform self-consistent Hartree-Fock calculations. The sublattice projection introduces an extra variational parameter l that has the physical meaning of a localization length for charge localized about a particular honeycomb-lattice site and that needs to be optimized. For given r_s and γ, we find the self-consistent solutions at each l. Then we compare solutions at different l and identify the one with lowest energy as the mean-field ground state whose pseudospin texture determines the sublattice structure and topology.

Figures 4(a) and 4(b) show the pseudospin textures of ground states at two different values of γ, corresponding respectively to a trivial WC state and a $C = 1$ AHC state. The charge density profiles in Figs. 4(c) and 4(d) make it clear that the WC state forms a triangular lattice while the AHC state forms a honeycomb lattice. Figure 4(e) shows the phase diagram in (r_s, γ) parameter space, where the color scale represents the localization length of the ground state. While the WC state is always the ground state when the form factor is trivial, a first-order transition to the AHC state occurs as γ increases. The critical value of γ increases with r_s.

Our sublattice-projected theory by construction does not consider melting of crystals into translationally invariant liquid phases. A useful approximate melting criterion is provided by the Lindemann criterion [57–60], which in our context states that melting occurs when the localization length l (in units of lattice constant a) reaches a critical

value. The color scale in Fig. 4(e) shows that the localization length of both WC and AHC states decreases with r_s. Although the precise critical value of l is unknown for the AHC state, since the phase boundary moves toward large r_s and small l as γ increases, we expect that at large γ the AHC state is stabilized as an intermediate phase between the WC and Fermi liquid phases. Following the contour line in Fig. 4(e) that starts from the critical $r_s^* \approx 30$ at $\gamma = 0$ [3,4], we obtain the schematic phase diagram in Fig. 1.

Discussion.—In this Letter we used a simple model to demonstrate the possibility of spontaneous crystallization of 2D electron systems into a topologically nontrivial state. Our sublattice pseudospin picture qualitatively explains the physical origin of the AHC states proposed by recent theoretical work [42–46], but goes beyond the context of multilayer graphene. Our theory shows that the most essential ingredient for AHCs is a nontrivial form factor $\Lambda_{\boldsymbol{p}',\boldsymbol{p}}$ with Berry curvature concentrated on the scale of the superlattice mBZ that breaks the effective TRS and favors a topologically nontrivial sublattice pseudospin texture. Nontrivial form factors also weaken the ferromagnetic exchange coupling that favors sublattice-polarized states and thus further stabilizes the AHC state.

An interesting open question is the optimal form of $\Lambda_{\boldsymbol{p}',\boldsymbol{p}}$ for the realization of AHCs. Our calculations at different winding numbers N show that the AHC area in the phase diagram does not monotonically increase with the Berry flux in the first mBZ. Figure 4(f) shows the critical value of γ for the transition from WC to AHC states at $N = 3, 4, 5, 6$ with fixed $r_s = 20$. At $N = 1$, 2, and 7, the WC state remains the ground state up to very large γ. Analytic progress on the h and J coefficients (see expressions in Supplemental Material [49]) or analogous studies using the controlled quantum geometry of ideal bands [61–63] can shed light on this nonmonotonic behavior and help identify the optimal form of $\Lambda_{\boldsymbol{p}',\boldsymbol{p}}$ as well as promising material candidates for the realization of AHCs.

Since all electrons in the WC state are well localized, the WC state is well described by the Slater determinant (3) and its total energy is largely independent of the specific form of sublattice basis orbitals we use as long as it has the correct localization length. For the AHC state, on the other hand, it is less clear whether the ansatz (3) and the sublattice basis construction provide an accurate description; if not, our calculations overestimate the energy of AHCs. Therefore, the critical γ in our results should be regarded as an upper bound for the realistic value. More sophisticated computational techniques such as quantum Monte Carlo methods are required to obtain a more accurate phase diagram.

Y. Z. thanks Allan MacDonald for very helpful discussion on pseudospin order in graphene. Y. Z. and A. J. M. acknowledge support from Programmable Quantum Materials, an Energy Frontiers Research Center funded by the U.S. Department of Energy (DOE), Office of Science, Basic Energy Sciences (BES), under Award No. DE-SC0019443. J. C. acknowledges support from the Air Force Office of Scientific Research under Grant No. FA9550-20-1-0260 and is partially supported by the Alfred P. Sloan Foundation through a Sloan Research Fellowship. The Flatiron Institute is a division of the Simons Foundation.

*yz4788@columbia.edu

[1] E. Wigner, On the interaction of electrons in metals, Phys. Rev. **46**, 1002 (1934).
[2] L. Bonsall and A. A. Maradudin, Some static and dynamical properties of a two-dimensional Wigner crystal, Phys. Rev. B **15**, 1959 (1977).
[3] B. Tanatar and D. M. Ceperley, Ground state of the two-dimensional electron gas, Phys. Rev. B **39**, 5005 (1989).
[4] N. D. Drummond and R. J. Needs, Phase diagram of the low-density two-dimensional homogeneous electron gas, Phys. Rev. Lett. **102**, 126402 (2009).
[5] B. Spivak and S. A. Kivelson, Phases intermediate between a two-dimensional electron liquid and Wigner crystal, Phys. Rev. B **70**, 155114 (2004).
[6] M. Zarenia, D. Neilson, B. Partoens, and F. M. Peeters, Wigner crystallization in transition metal dichalcogenides: A new approach to correlation energy, Phys. Rev. B **95**, 115438 (2017).
[7] V. J. Goldman, M. Santos, M. Shayegan, and J. E. Cunningham, Evidence for two-dimentional quantum Wigner crystal, Phys. Rev. Lett. **65**, 2189 (1990).
[8] J. Yoon, C. C. Li, D. Shahar, D. C. Tsui, and M. Shayegan, Wigner crystallization and metal-insulator transition of two-dimensional holes in gaas at $B = 0$, Phys. Rev. Lett. **82**, 1744 (1999).
[9] M. S. Hossain, M. Ma, K. V. Rosales, Y. Chung, L. Pfeiffer, K. West, K. Baldwin, and M. Shayegan, Observation of spontaneous ferromagnetism in a two-dimensional electron system, Proc. Natl. Acad. Sci. U.S.A. **117**, 32244 (2020).
[10] Y. Zhou, J. Sung, E. Brutschea, I. Esterlis, Y. Wang, G. Scuri, R. J. Gelly, H. Heo, T. Taniguchi, K. Watanabe *et al.*, Bilayer Wigner crystals in a transition metal dichalcogenide heterostructure, Nature (London) **595**, 48 (2021).
[11] T. Smoleński, P. E. Dolgirev, C. Kuhlenkamp, A. Popert, Y. Shimazaki, P. Back, X. Lu, M. Kroner, K. Watanabe, T. Taniguchi *et al.*, Signatures of Wigner crystal of electrons in a monolayer semiconductor, Nature (London) **595**, 53 (2021).
[12] H. Li, S. Li, E. C. Regan, D. Wang, W. Zhao, S. Kahn, K. Yumigeta, M. Blei, T. Taniguchi, K. Watanabe *et al.*, Imaging two-dimensional generalized Wigner crystals, Nature (London) **597**, 650 (2021).
[13] E. C. Regan, D. Wang, C. Jin, M. I. Bakti Utama, B. Gao, X. Wei, S. Zhao, W. Zhao, Z. Zhang, K. Yumigeta *et al.*, Mott and generalized Wigner crystal states in WSe_2/WS_2 moiré superlattices, Nature (London) **579**, 359 (2020).
[14] Z. Xiang, H. Li, J. Xiao, M. H. Naik, Z. Ge, Z. He, S. Chen, J. Nie, S. Li, Y. Jiang *et al.*, Quantum melting of a disordered Wigner solid, arXiv:2402.05456.

[15] C.-Z. Chang, C.-X. Liu, and A. H. MacDonald, Colloquium: Quantum anomalous Hall effect, Rev. Mod. Phys. **95**, 011002 (2023).
[16] F. D. M. Haldane, Model for a quantum Hall effect without Landau levels: Condensed-matter realization of the "parity anomaly", Phys. Rev. Lett. **61**, 2015 (1988).
[17] C.-Z. Chang, J. Zhang, X. Feng, J. Shen, Z. Zhang, M. Guo, K. Li, Y. Ou, P. Wei, L.-L. Wang *et al.*, Experimental observation of the quantum anomalous Hall effect in a magnetic topological insulator, Science **340**, 167 (2013).
[18] C.-Z. Chang, W. Zhao, D. Y. Kim, H. Zhang, B. A. Assaf, D. Heiman, S.-C. Zhang, C. Liu, M. H. Chan, and J. S. Moodera, High-precision realization of robust quantum anomalous Hall state in a hard ferromagnetic topological insulator, Nat. Mater. **14**, 473 (2015).
[19] Y. Deng, Y. Yu, M. Z. Shi, Z. Guo, Z. Xu, J. Wang, X. H. Chen, and Y. Zhang, Quantum anomalous Hall effect in intrinsic magnetic topological insulator $MnBi_2Te_4$, Science **367**, 895 (2020).
[20] T. Li, S. Jiang, B. Shen, Y. Zhang, L. Li, Z. Tao, T. Devakul, K. Watanabe, T. Taniguchi, L. Fu *et al.*, Quantum anomalous Hall effect from intertwined moiré bands, Nature (London) **600**, 641 (2021).
[21] Z. Tao, B. Shen, S. Jiang, T. Li, L. Li, L. Ma, W. Zhao, J. Hu, K. Pistunova, K. Watanabe, T. Taniguchi, T. F. Heinz, K. F. Mak, and J. Shan, Valley-coherent quantum anomalous Hall state in AB-stacked $MoTe_2/WSe_2$ bilayers, Phys. Rev. X **14**, 011004 (2024).
[22] M. Serlin, C. Tschirhart, H. Polshyn, Y. Zhang, J. Zhu, K. Watanabe, T. Taniguchi, L. Balents, and A. Young, Intrinsic quantized anomalous Hall effect in a moiré heterostructure, Science **367**, 900 (2020).
[23] T. Han, Z. Lu, G. Scuri, J. Sung, J. Wang, T. Han, K. Watanabe, T. Taniguchi, H. Park, and L. Ju, Correlated insulator and Chern insulators in pentalayer rhombohedral stacked graphene, Nat. Nanotechnol. **19**, 181 (2024).
[24] Z. Lu, T. Han, Y. Yao, A. P. Reddy, J. Yang, J. Seo, K. Watanabe, T. Taniguchi, L. Fu, and L. Ju, Fractional quantum anomalous Hall effect in multilayer graphene, Nature (London) **626**, 759 (2024).
[25] T. Han, Z. Lu, Y. Yao, J. Yang, J. Seo, C. Yoon, K. Watanabe, T. Taniguchi, L. Fu, F. Zhang *et al.*, Large quantum anomalous Hall effect in spin-orbit proximitized rhombohedral graphene, Science **384**, 647 (2024).
[26] F. Wu, T. Lovorn, E. Tutuc, I. Martin, and A. H. MacDonald, Topological insulators in twisted transition metal dichalcogenide homobilayers, Phys. Rev. Lett. **122**, 086402 (2019).
[27] T. Devakul, V. Crépel, Y. Zhang, and L. Fu, Magic in twisted transition metal dichalcogenide bilayers, Nat. Commun. **12**, 6730 (2021).
[28] V. Crépel and L. Fu, Anomalous Hall metal and fractional Chern insulator in twisted transition metal dichalcogenides, Phys. Rev. B **107**, L201109 (2023).
[29] Y. Zeng, T. M. R. Wolf, C. Huang, N. Wei, S. A. A. Ghorashi, A. H. MacDonald, and J. Cano, Gate-tunable topological phases in superlattice modulated bilayer graphene, Phys. Rev. B **109**, 195406 (2024).
[30] T. Tan, A. P. Reddy, L. Fu, and T. Devakul, Designing topology and fractionalization in narrow gap semiconductor films via electrostatic engineering, arXiv:2402.03085.
[31] Y. Su, H. Li, C. Zhang, K. Sun, and S.-Z. Lin, Massive dirac fermions in moiré superlattices: A route towards topological flat minibands and correlated topological insulators, Phys. Rev. Res. **4**, L032024 (2022).
[32] N. Suri, C. Wang, B. M. Hunt, and D. Xiao, Superlattice engineering of topology in massive Dirac fermions, Phys. Rev. B **108**, 155409 (2023).
[33] V. Crépel, A. Dunbrack, D. Guerci, J. Bonini, and J. Cano, Chiral model of twisted bilayer graphene realized in a monolayer, Phys. Rev. B **108**, 075126 (2023).
[34] O. P. Sushkov and A. H. Castro Neto, Topological insulating states in laterally patterned ordinary semiconductors, Phys. Rev. Lett. **110**, 186601 (2013).
[35] H. D. Scammell and O. P. Sushkov, Tuning the topological insulator states of artificial graphene, Phys. Rev. B **99**, 085419 (2019).
[36] S. Raghu, X.-L. Qi, C. Honerkamp, and S.-C. Zhang, Topological Mott insulators, Phys. Rev. Lett. **100**, 156401 (2008).
[37] T. Liu, B. Douçot, and K. Le Hur, Realizing topological Mott insulators from the RKKY interaction, Phys. Rev. B **93**, 195153 (2016).
[38] S. Capponi and A. M. Läuchli, Phase diagram of interacting spinless fermions on the honeycomb lattice: A comprehensive exact diagonalization study, Phys. Rev. B **92**, 085146 (2015).
[39] A. G. Grushin, E. V. Castro, A. Cortijo, F. de Juan, M. A. H. Vozmediano, and B. Valenzuela, Charge instabilities and topological phases in the extended Hubbard model on the honeycomb lattice with enlarged unit cell, Phys. Rev. B **87**, 085136 (2013).
[40] B. I. Halperin, Z. Tešanović, and F. Axel, Compatibility of crystalline order and the quantized Hall effect, Phys. Rev. Lett. **57**, 922 (1986).
[41] Z. Tešanović, F. Axel, and B. I. Halperin, "Hall crystal" versus Wigner crystal, Phys. Rev. B **39**, 8525 (1989).
[42] J. Dong, T. Wang, T. Wang, T. Soejima, M. P. Zaletel, A. Vishwanath, and D. E. Parker, Anomalous Hall crystals in rhombohedral multilayer graphene I: Interaction-driven Chern bands and fractional quantum Hall states at zero magnetic field, arXiv:2311.05568.
[43] Z. Dong, A. S. Patri, and T. Senthil, Theory of fractional quantum anomalous Hall phases in pentalayer rhombohedral graphene moiré structures, arXiv:2311.03445.
[44] B. Zhou, H. Yang, and Y.-H. Zhang, Fractional quantum anomalous Hall effects in rhombohedral multilayer graphene in the moiréless limit and in Coulomb imprinted superlattice, arXiv:2311.04217.
[45] Z. Guo, X. Lu, B. Xie, and J. Liu, Theory of fractional Chern insulator states in pentalayer graphene moiré superlattice, arXiv:2311.14368.
[46] Y. H. Kwan, J. Yu, J. Herzog-Arbeitman, D. K. Efetov, N. Regnault, and B. A. Bernevig, Moiré fractional Chern insulators III: Hartree-Fock phase diagram, magic angle regime for Chern insulator states, the role of the moiré potential and Goldstone gaps in rhombohedral graphene superlattices, arXiv:2312.11617.
[47] Note that $\mathcal{T}$ is not the physical time-reversal operator, but rather an antiunitary operator that acts like time reversal within a single valley. The complete physical system

contains another valley that is the physical time-reversal partner of the band we describe and transforms differently under the effective time reversal $\mathcal{T}$, but we assume it is at higher energy due to either explicit or spontaneous breaking of the physical time-reversal symmetry.

[48] Throughout this Letter, by TRS we always refer to the effective time-reversal symmetry that acts within a single valley.

[49] See Supplemental Material at http://link.aps.org/supplemental/10.1103/PhysRevLett.132.236601, which includes Refs. [50–52], for extended results and methodology.

[50] N. Marzari and D. Vanderbilt, Maximally localized generalized Wannier functions for composite energy bands, Phys. Rev. B **56**, 12847 (1997).

[51] I. Souza, N. Marzari, and D. Vanderbilt, Maximally localized Wannier functions for entangled energy bands, Phys. Rev. B **65**, 035109 (2001).

[52] N. Marzari, A. A. Mostofi, J. R. Yates, I. Souza, and D. Vanderbilt, Maximally localized Wannier functions: Theory and applications, Rev. Mod. Phys. **84**, 1419 (2012).

[53] A. H. MacDonald, J. Jung, and F. Zhang, Pseudospin order in monolayer, bilayer and double-layer graphene, Phys. Scr. **2012**, 014012 (2012).

[54] H. Min, G. Borghi, M. Polini, and A. H. MacDonald, Pseudospin magnetism in graphene, Phys. Rev. B **77**, 041407(R) (2008).

[55] While the precise value of d does not affect the qualitative physics we discuss, our choice is motivated by rhombohedral graphene moiré devices where the moiré length is around 10–15 nm. Since the relevant r_s is around 20–30, our choice gives the typical gate distance $d = 20$–30 nm.

[56] Note that this is not a general result for any form factors. For example, for $N = 1$ both $\boldsymbol{h}^{\mathrm{HF}}$ and $J \cdot n^{\mathrm{kin}}$ favor $C = +1$. See Supplemental Material for results at other winding numbers [49].

[57] S. A. Khrapak, Lindemann melting criterion in two dimensions, Phys. Rev. Res. **2**, 012040(R) (2020).

[58] X. Zheng and J. Earnshaw, On the Lindemann criterion in 2D, Europhys. Lett. **41**, 635 (1998).

[59] V. Bedanov, G. Gadiyak, and Y. E. Lozovik, On a modified Lindemann-like criterion for 2D melting, Phys. Lett. A **109**, 289 (1985).

[60] G. Goldoni and F. M. Peeters, Stability, dynamical properties, and melting of a classical bilayer Wigner crystal, Phys. Rev. B **53**, 4591 (1996).

[61] J. Wang, J. Cano, A. J. Millis, Z. Liu, and B. Yang, Exact Landau level description of geometry and interaction in a flatband, Phys. Rev. Lett. **127**, 246403 (2021).

[62] B. Estienne, N. Regnault, and V. Crépel, Ideal Chern bands as Landau levels in curved space, Phys. Rev. Res. **5**, L032048 (2023).

[63] V. Crépel, N. Regnault, and R. Queiroz, Chiral limit and origin of topological flat bands in twisted transition metal dichalcogenide homobilayers, Commun. Phys. **7**, 146 (2024).